Evaluation of a full-scale helium-filled soap bubble generator

Bradley Gibeau[1], Drew Gingras[1], and Sina Ghaemi[1†]

[1] Department of Mechanical Engineering, University of Alberta, Edmonton, Alberta T6G 2R3, Canada
[†] ghaemi@ualberta.ca

Abstract

Various aspects of the design and operation of a full-scale helium-filled soap bubble (HFSB) generator are studied. Shadowgraphy, particle image/tracking velocimetry, hotwire anemometry, and Monte Carlo simulations are employed to investigate bubble production regimes, diameters, production rates, time responses, and the flow quality downstream from the full-scale system. Modifications to internal nozzle geometry are found to greatly impact the production regimes that the nozzles operate within. Specifically, improving the axisymmetry of the air flow within a nozzle leads to desirable bubble formation over a larger range of input combinations and the ability to operate at larger input rates in general. The input of bubble film solution (BFS) is also found to be important for ensuring proper operation, as both small and large inputs lead to undesirable production. A previously defined theoretical relationship (Faleiros et al., Exp Fluids 60:40, 2019) between input parameters and the mean bubble time response is confirmed but found to vary depending on nozzle operation, as spilled BFS and leaked helium during bubble formation cause deviation from theoretical operation. Monte Carlo simulations reveal that the spatial filtering of particle image velocimetry (PIV) reduces the standard deviation of the effective distribution of the bubble time responses by a factor of $\mathrm{PPIR}^{-1/2}$, where PPIR is the number of particles per interrogation region. This power law is used to derive an equation for estimating the minimum time scale of the flow that can be resolved using the bubbles from a given generator during applications of PIV. Finally, the wind tunnel flow downstream from a full-scale generator is found to be affected by the blockage of the structure, with the freestream deficit increasing by at most 1.2% of the mean and the freestream turbulence intensity increasing by at most 0.3% for freestream velocities of 6 m/s or greater.

1 Introduction

Helium-filled soap bubbles (HFSBs) can be used as tracers for large-scale visualizations and measurements in air provided that their tracing fidelity can be adequately controlled (Bosbach et al. 2009; Scarano et al. 2015). Their larger diameters (~0.5 mm) allow for orders of magnitude more light to be scattered when compared to typical tracer particles used in air (~1 μm), as light scattering scales with the square of particle diameter (Raffel et al. 2018). In the case of particle image velocimetry (PIV) and particle tracking velocimetry (PTV), typical tracers limit the volumetric domain of the measurements to the order of 10 cm^3 when current imaging and illumination technology are used (Scarano 2013). When HFSBs are employed as tracers, measurements in volumes on the order of cubic meters are attainable (e.g. Huhn et al. 2017). This is vital for the application of PIV and PTV for large-scale wind tunnel measurements.

One difficulty associated with using HFSB generators is ensuring that the resulting bubbles have good tracing fidelity. The tracing fidelity of a particle is quantified using the particle time response. In general, it is recommended that the time response be an order of magnitude smaller than the time scale of the fluctuations that the particle is meant to track (Tropea et al. 2007). The time response is primarily dictated by the density of the particle in relation to that of the surrounding fluid. A particle that is denser than the surrounding fluid will lag the true acceleration of a flow field, and a buoyant particle will lead the true acceleration. Neither is desirable when conducting measurements. Knowledge of the distribution of time responses associated with HFSBs is therefore critical for designing reliable experiments.

HFSBs were used for qualitative flow visualizations before their time responses could be adequately controlled (e.g. Hale et al. 1971), and early investigations into their tracing fidelity yielded

undesirable results (Kerho and Bragg 1994). However, later experiments showed that producing HFSBs with adequate tracing fidelity for wind tunnel experiments was possible (Scarano et al. 2015). Other investigations have since reproduced this conclusion as well (Gibeau and Ghaemi 2018; Faleiros et al. 2018, 2019).

Faleiros et al. (2018, 2019) made use of a single orifice-type (Bosbach et al. 2009) HFSB nozzle and measured the time response of the resulting bubbles in the deceleration field leading up to the front stagnation point of a circular cylinder. They were able to achieve HFSBs that were neutrally buoyant on average, and the standard deviations of the resulting distributions of time responses were found to range approximately from 20 to 70 μs. Gibeau and Ghaemi (2018) utilized a 3D-printed 8-nozzle (also orifice-type) system, which better represented the complexity and added uncertainties of a large-scale HFSB generator that is necessary for wind tunnel measurements. They performed a similar cylinder experiment to measure the time response of the bubbles from the multi-nozzle system and achieved bubbles that were neutrally buoyant on average, but with a larger distribution of time responses featuring a standard deviation of 171 μs. The larger standard deviation of time responses was accompanied by a larger distribution of bubbles sizes. These differences were attributed to the difficulties associated with regulating equal input flow rates to each nozzle in the multi-nozzle system and to small differences between each of the nozzles. Despite this, Gibeau and Ghaemi (2018) concluded that the system can produce bubbles that will track velocity fluctuations with a characteristic time scale of 5 ms or greater, which is suitable for many large-scale wind tunnel experiments.

The evaluation of the measurable characteristic time scale associated with a HFSB generator performed by Gibeau and Ghaemi (2018) was based on the performance of individual bubbles and therefore applies to PTV measurements. However, performing PIV using HFSBs in wind tunnels, especially tomographic PIV (Elsinga et al. 2006), is a common goal that researchers have been working towards. In the case of PIV, groups of particles each with different time responses are correlated to obtain velocity vectors. A relevant question can then be asked pertaining to HFSBs produced with a given distribution of time responses: how does the effective time response distribution change when groups of particles are correlated? This question is addressed in the present work.

A second difficulty associated with using HFSBs as tracers is producing sufficient seeding densities for experiments. In the past this issue has been coped with by tracking sparse amounts of bubbles (Müller et al. 2001; Caridi et al. 2017; Faleiros et al. 2018), conducting measurements in enclosed spaces where bubbles can accumulate (Bosbach et al. 2009; Kühn et al. 2011; Huhn et al. 2017; Terra et al. 2017), or by collecting bubbles over time and releasing them at once (Scarano et al. 2015; Caridi et al. 2016). Only recent investigations have considered multi-nozzle generators placed directly into a wind tunnel. For example, the modular system proposed by Gibeau and Ghaemi (2018) and the wing-based system utilized by Jux et al. (2018).

Maximizing the bubble production of a single nozzle is one step towards obtaining sufficient seeding densities in wind tunnels. Gibeau and Ghaemi (2018) measured production rates by counting the number of bubbles in a volume downstream from their generator. They found that production rates were dictated primarily by the flow of bubble film solution (BFS) into the nozzles. A doubling of production rates was observed when the input of BFS was doubled for certain cases, suggesting that BFS was a limiting factor. Faleiros et al. (2019) measured production rates directly at the exit of their nozzle using shadowgraphy by considering the distance between adjacent bubbles and their velocities. They concluded that the air input dominated production rates, and that increasing BFS led to a decrease in production in all cases. These conflicting results motivate comparison of the differences between the generators used in these studies, of which there are two: internal nozzle geometry and nozzle operating orientation. The effects of these considerations have not been investigated in the literature to date. Additionally, only Faleiros et al. (2019) considered the different production regimes that a nozzle operates within. They found that there were two primary production regimes: bubbling and jetting. Bubbling refers to bubble production that is internal to the nozzle, while jetting refers to when bubbles form external to the nozzle via a jet of helium and BFS. The production rate trends of Faleiros et al. (2019) only considered operation in the bubbling regime and it was not known which regime the nozzles of Gibeau and Ghaemi (2018) were operating in. This is another possible reason for the discrepancy in production rate trends reported by the two investigations.

A typical HFSB nozzle can produce roughly 50,000 bubbles/s (Gibeau and Ghaemi 2018; Faleiros et al. 2019), which is not sufficient for wind tunnel experiments. For example, a tomographic PIV measurement in a wind tunnel at 20 m/s may require 5 bubbles/cm^3 and a HFSB streamtube with

a 20×20 cm^2 cross-sectional area. It would take a minimum of 80 nozzles producing at 50,000 bubbles/s to satisfy these requirements. If the desired seeding density, freestream velocity, or either of the streamtube dimensions are altered, the number of required nozzles will change linearly. It is therefore necessary to scale up to large, multi-nozzle systems in order to conduct PIV measurements in a wind tunnel using HFSBs.

Recently, Jux et al. (2018) employed a multi-wing seeding rake to allow for the use of 80 HFSB nozzles in a wind tunnel environment. The system was estimated to provide ~1 bubble/cm^3 in a cross-section with dimensions of 15×48 cm^2 at 14.0 m/s. In such a wing-based system, the nozzles are located at the trailing edge of each wing, which only allows for a single nozzle at each location in the streamtube plane. This limits the seeding density at each location to what can be produced by a single nozzle, and also places an upper limit on the velocities that can be adequately seeded. A solution to this problem was presented by Gibeau and Ghaemi (2018), who utilized a modular system for arranging their HFSB nozzles vertically pointing downwards. Each module allowed for aligning nozzles in series at a given location in the streamtube plane. The 8 nozzles resulted in a seeding density of 1.6 bubbles/cm^3 in a streamtube with dimensions of 15×15 cm^2 at 10.3 m/s. This highlighted the benefits of placing nozzles in series to achieve higher seeding densities with full-scale systems.

The need for multi-nozzle HFSB generators is accompanied by yet another consideration that has the potential to affect measurement quality, and that is the impact that the nozzle support structure has on the test-section flow quality. This was briefly investigated by Jux et al. (2018), but the full-scale generator was not the focus of their study. They found that their multi-wing generator imposed a negligible deficit on the mean flow, and that the turbulence intensity downstream was at most 1.9%. The impact of the modular generator on the mean flow quality was not investigated by Gibeau and Ghaemi (2018).

The above discussion reveals that there are a few uncertainties surrounding the design and operation of full-scale HFSB generators. Regarding single nozzles, the impact of modifying internal nozzle geometry and operating orientation are unknown, as are the production rate trends for the jetting regime. Considering full-scale systems, the flow quality downstream from a large HFSB generator has only been briefly investigated, and the effective tracing fidelity for correlation-based techniques has not yet been studied. The present investigation seeks to further the current understanding of these uncertainties. The primary topics are as follows:

(i) The effect of modifying internal nozzle geometry on the performance of an orifice-type HFSB nozzle. We compare the performance of three 3D-printed nozzles with different internal geometries, including the design employed by Gibeau and Ghaemi (2018). Comparison with the results of Faleiros et al. (2019) will be made where possible as well, as their nozzle geometry is also different.

(ii) How nozzle performance varies with operating orientation. One of the three nozzle geometries is selected, and the differences between vertical and horizontal operation are studied.

(iii) Production regime transitions. The variability and transition of the production regimes that the three nozzles are capable of are studied and compared to those reported by Faleiros et al. (2019).

(iv) Theoretical analysis of effective time response. Monte Carlo simulations are employed to draw conclusions regarding effective time response distributions for applications of PIV.

(v) The impact of a large HFSB generator on the freestream flow quality in a wind tunnel. The mean freestream deficit and turbulence intensities imposed by a modular HFSB generator are quantified for ten freestream velocities.

The topics mentioned above are investigated using a combination of shadowgraphy, PTV, PIV, hotwire anemometry, and Monte Carlo simulation.

2 The modular HFSB generator

2.1 Nozzle design

The basic nozzle design was developed using initial descriptions of orifice-type nozzles provided by Bosbach et al. (2009). The first nozzle considered is the same design used by Gibeau and Ghaemi (2018). The second and third nozzles are modified versions of the first. Schematics of all three are presented in Fig. 1. Each nozzle functions using the same basic principles. Concentric flows of bubble film solution (BFS) and helium (He) form a jet of BFS with a He core within the cavity of the nozzle. The outer flow of air acts to force the jet through the orifice at the end of the cavity where the BFS jet disintegrates to form individual bubbles.

Each nozzle consists of two primary components: a body and a cap. Both were 3D-printed using a Formlabs 3D printer (Form 2). The orifice in each cap is 0.85 mm in diameter. As is visible in Fig.

1, the body and cap of each nozzle are secured together using locking tabs and an o-ring. The locking tabs of the body slide into axial grooves in the cap. The cap is then turned to lock the two components together. The other nozzle components include 16-guage stainless steel tubing (OD = 1.65 mm, ID = 1.35 mm) and a blunt 22-gauge syringe needle (OD = 0.71 mm, ID = 0.48 mm). The syringe needle is used as the He inlet, while all other tubing components in Fig. 1 are made from the 16-gauge stock. All tubing components were fixed in place using an adhesive.

As previously mentioned, Nozzle 2 and Nozzle 3 are modified versions of Nozzle 1. The modified cap of Nozzle 2 features a small ring groove to allow the air to spread more evenly within the nozzle. The body of Nozzle 3 features a similar modification to allow for air circulation, but it is much larger. Both modifications were made with the goal of promoting the concentricity of the internal flows as the air inlet in the current design is perpendicular to the nozzle outlet.

2.2 Full-scale system

The full-scale system has also been developed using a 3D printer and is an extension of the modular system proposed by Gibeau and Ghaemi (2018). The current version features two vertical supports with NACA 0012 cross-sections to reduce their downstream flow disturbance. The height of each vertical support is adjustable, as are the module mounting locations. Each module is a rectangular duct that allows for nozzles to be fixed to the top, pointing vertically downward into the duct, in any desirable arrangement. The nozzles generate HFSBs into each duct, and the freestream flow carries the resulting streamtube to the test section. A schematic and photograph of the current modular system are shown in Fig. 2. The arrangement in the photograph features 4 modules, each with 8 nozzles. Each location in the streamtube plane is seeded by 4 nozzles in series. The size, location, and nozzle arrangement of each duct can be modified to achieve the correct seeding density and streamtube dimensions for a given experiment. The entire structure with the arrangement shown in Fig. 2 has a total frontal area of 0.125 m^2 (excluding the tubing), which corresponds to a blockage of less than 1% in the settling chamber of the wind tunnel used in this study. The tubing visible in Fig. 2 is exposed for practical reasons. It is necessary to be able to check for leaks/blockages, replace faulty nozzles, prime the soap lines, etc., while using the system. A future version of the full-scale design may feature a streamlined enclosure for the tubing.

Each nozzle is supplied with air, He, and BFS through 1/8-inch flexible tubing, which is fed through the internal cavity of each NACA 0012 profile. The flow of BFS (Sage Action Inc., 1035) is regulated using one or more multi-syringe pumps. The flows of air and He are regulated using one digital flow controller for each fluid. These flows are directed through a series of axisymmetric distribution manifolds to promote equal flowrates to each of the nozzles in the multi-nozzle system. Each manifold is a cylindrical disk. The inlet is located at one of the flat faces of the cylinder and the outlets are located radially along the outer curved surface. These manifolds have been designed to achieve equal pressure drop at each outlet. One primary manifold distributes the flows to secondary manifolds that are associated with each module. The outlets of the secondary manifolds then feed directly to each nozzle.

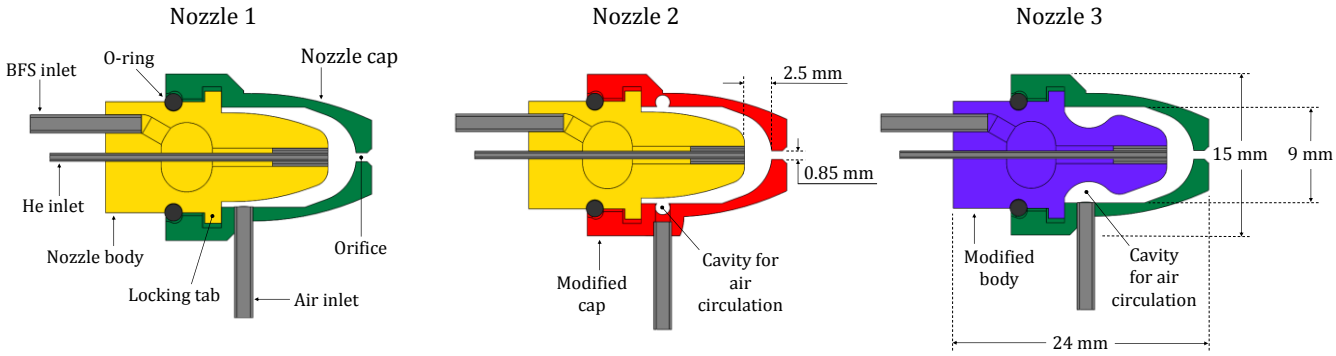

Fig. 1 Schematics of the three nozzle designs. Nozzle 1 is the same nozzle utilized by Gibeau and Ghaemi (2018). The schematics are to scale, and all labelled dimensions are constant across the three designs.

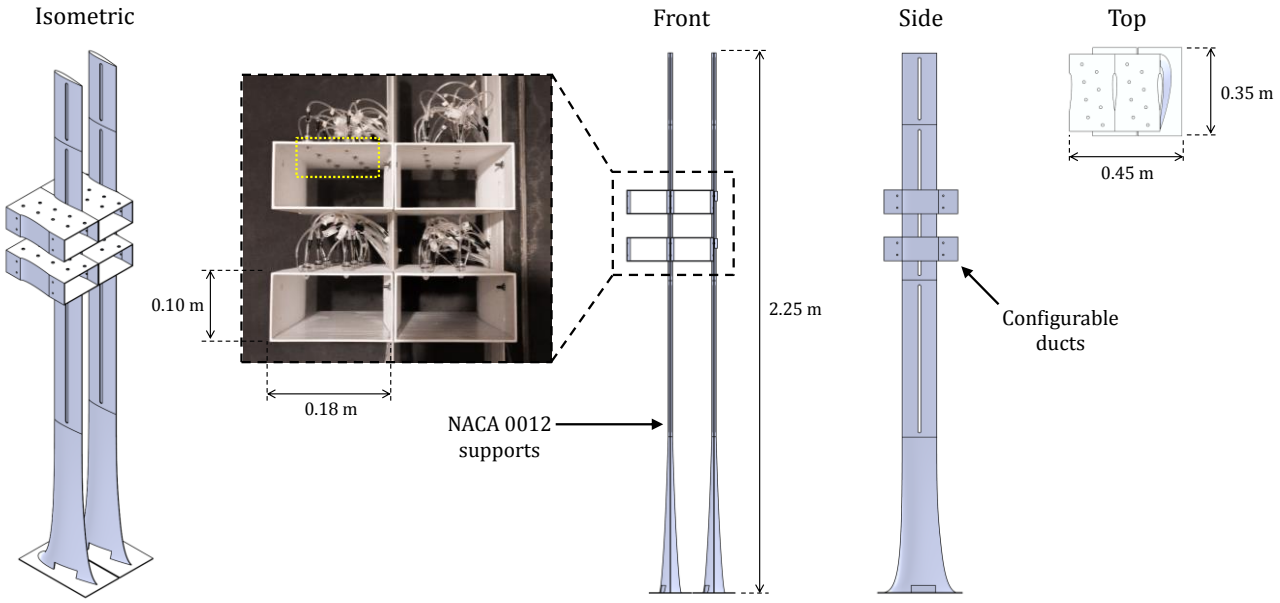

Fig. 2 Three-dimensional schematic of the full-scale system and photograph of the front view. The yellow dotted box in the photograph highlights the vertically mounted nozzles pointing downwards into a duct.

3 Experiments

The bubble formation has been characterized at the exit of the nozzles using shadowgraphy, allowing for analysis of the nozzle production regimes, bubble sizes, and production rates in some cases. The time response of the bubbles was measured in a wind tunnel by comparing the bubble dynamics to the true flow field within an induced deceleration field. This was carried out using PTV and PIV for the bubbles and true flow field, respectively. Finally, the mean flow quality was characterized in a wind tunnel downstream from the full-scale generator. PIV and hotwire anemometry were applied to measure the freestream uniformity and turbulence intensities, respectively. These experiments are described in detail next.

3.1 Shadowgraphy of bubble formation

Shadowgraphy was conducted at the exit of each nozzle using an Imager Intense camera featuring a 1376×1040-pixel CCD sensor with a 6.45×6.45 μm² pixel size and 12-bit resolution. Illumination was provided by a dual-cavity Nd:YAG laser (New Wave Research, Solo PIV III) capable of producing 532 nm light at 50 mJ per pulse at a 15 Hz repetition rate. A diffuser was attached to the output of the laser to obtain diffused backlight illumination. A 12× Navitar zoom lens was used to obtain a resolution of 18.2 μm/pix in a field of view (FOV) of 15.1×6.4 mm², which was cropped to increase the acquisition frequency of the camera.

The volumetric flowrates for air ($\dot{V}_{\mathrm{Air}}$), He ($\dot{V}_{\mathrm{He}}$), and BFS ($\dot{V}_{\mathrm{BFS}}$) were varied in the ranges $0.50 \leq \dot{V}_{\mathrm{Air}} \leq 1.75$ L/min, $0.06 \leq \dot{V}_{\mathrm{He}} \leq 0.26$ L/min, and $7 \leq \dot{V}_{\mathrm{BFS}} \leq 13$ mL/h, respectively, for a total of 144 operating points for each nozzle. A multi-syringe pump (World Precisions Instruments, AL-8000) was used to regulate $\dot{V}_{\mathrm{BFS}}$. Two digital flow controllers were used to regulate $\dot{V}_{\mathrm{Air}}$ (Cole-Parmer, model # 32907-71) and $\dot{V}_{\mathrm{He}}$ (Cole-Parmer, model # 32907-57). The production of Nozzle 1 and Nozzle 2 was imaged while the nozzles were oriented vertically pointing downwards, whereas Nozzle 3 was imaged both vertically and horizontally. Ensembles of 600 double-frame images were collected over a period of 1 minute for each case, resulting in 576 considered operating cases in total.

The resulting shadowgraphy images were analyzed three different ways. First, qualitative inspection of all cases was used to determine the production regimes of the nozzles for each input flowrate combination. Second, the images were processed using the particle sizing feature of DaVis 8.4 (LaVision GmbH) to determine the HFSB size distributions and to estimate bubble velocity from the double-frame images. A minimum centricity of 85% was enforced, and no restriction on particle size was imposed. Finally, following the method of

Faleiros et al. (2019), the production rates ($\dot{N}$) of select cases were estimated using the velocity of the bubbles (u_b) at the exit of the nozzle and the mean distance between adjacent bubbles (λ):

$$\dot{N} = \frac{u_b}{\lambda}. \quad (1)$$

3.2 Particle tracking for time response

The time response measurements were carried out in a two-story, closed-loop wind tunnel that is capable of flow speeds up to 35 m/s. Screens and honeycombs condition the flow at the entrance of the settling chamber, which contracts at a ratio of 6.3:1 leading to the test section with dimensions of 2.4×1.2 m² (W×H). A general schematic of the wind tunnel experiment is presented in Fig. 3.

A single module with 8 nozzles was used to provide a better estimate of the time response distributions resulting from a multi-nozzle system. The same multi-syringe pump and digital flow controller described in Section 3.1 were used to regulate $\dot{V}_{BFS}$ and $\dot{V}_{He}$, respectively. A 50 L/min digital flow controller (Omega, model # FMA-LP2609A) was used to regulate the larger $\dot{V}_{Air}$ required for 8 nozzles.

Using the technique applied by Scarano et al. (2015), Gibeau and Ghaemi (2018), and Faleiros et al. (2018, 2019), the time response was measured in a deceleration field leading up to a stagnation point. The deceleration in the present experiment was induced by a NACA 4418 airfoil at zero angle of attack. The model has a chord length of 0.975 m and was oriented vertically in the wind tunnel, spanning the entire 1.2-m height of the test section as is depicted in Fig. 3.

A Phantom v611 high-speed camera featuring a 1280×800-pixel CMOS sensor with a 20×20 μm² pixel size and 12-bit resolution was used to take time-resolved images of the HFSBs for tracking. Illumination was provided by a dual-cavity Nd:YLF laser (Photonics Industries, DM20-527-DH) capable of producing 527 nm light at 20 mJ per pulse at 1 kHz repetition rate. Higher repetition rates are possible at lower energy per pulse. Several optics were used to form a laser sheet with a thickness of 2 mm through the x-z FOV denoted as FOV1 in Fig. 3. FOV1 was located ~30 cm from the floor of the wind tunnel at the center of the HFSB streamtube. A 50-mm Nikon lens with an aperture setting of $f/4$ was used to obtain a cropped FOV of 196×196 mm² with a resolution of 245 μm/pix. The larger FOV was used to eliminate the doublet image patterns produced by

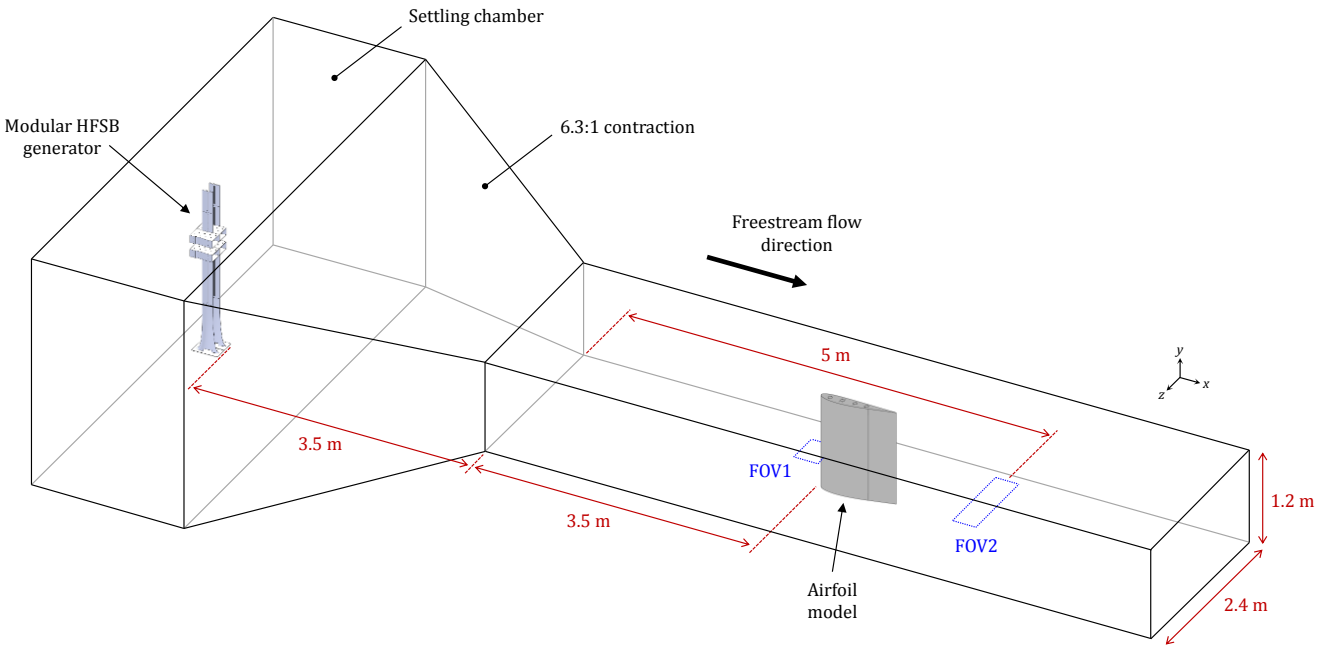

Fig. 3 Schematic of the overall wind tunnel configuration for experiments.

the large HFSBs at high magnification. The doublets can interfere with the tracking algorithm.

All time response experiments were conducted at a freestream velocity of 12.3 m/s. A set of 3900 double-frame images was recorded using standard 1-μm particles that were generated using a fog machine. This data forms the reference set to which all HFSB tracks are compared. Sets of 7800 single-frame images were recorded at an acquisition frequency of 6 kHz for the considered HFSB cases. DaVis 8.4 (LaVision GmbH) was used to process the images. The reference set was preprocessed by subtracting the ensemble minimum followed by normalizing with the ensemble average. A sum-of-correlation algorithm (Meinhart et al. 2000) was then applied using 24×24-pixel (5.9×5.9-mm) Gaussian interrogation windows with 75% overlap to obtain the reference mean velocity field. The time-resolved sets were processed using the DaVis 2D-PTV algorithm to obtain individual tracks. Bubbles were detected using a Gaussian 3×3 fit with a minimum intensity threshold of 250 counts. All tracks with lengths of less than 11 time steps were discarded.

The time response was calculated as the ratio of the slip velocity and bubble acceleration:

$$\tau = \frac{|\vec{U}_{\mathrm{ref}}| - |\vec{U}_{\mathrm{HFSB}}|}{|\vec{a}_{\mathrm{HFSB}}|} \qquad (2)$$

where the numerator, i.e. the slip velocity, is the difference between the reference velocity magnitude and the velocity magnitude of a HFSB, and the denominator is the acceleration magnitude of the same HFSB. The reference velocity at a given point has been obtained by linearly interpolating the reference velocity grid, while the velocity and acceleration of each HFSB has been obtained by fitting a second-order polynomial to the bubble locations obtained from PTV using a least-squares method. Eq. (2) was applied to all PTV tracks in a 30×30 mm^2 region beginning 35 mm upstream from the front stagnation point of the airfoil for each considered case. This region is shown relative to the streamlines of the reference flow and stagnation point in Fig. 4. This region was selected for its large deceleration and to ensure a sufficient number of tracks were measured for convergence of the results. Note that Eq. (2) assumes that $\vec{U}_{\mathrm{ref}}$ and $\vec{U}_{\mathrm{HFSB}}$ are in the same direction. This assumption is reasonable in the present application because the streamline deflection within the considered region in Fig. 4 is negligible.

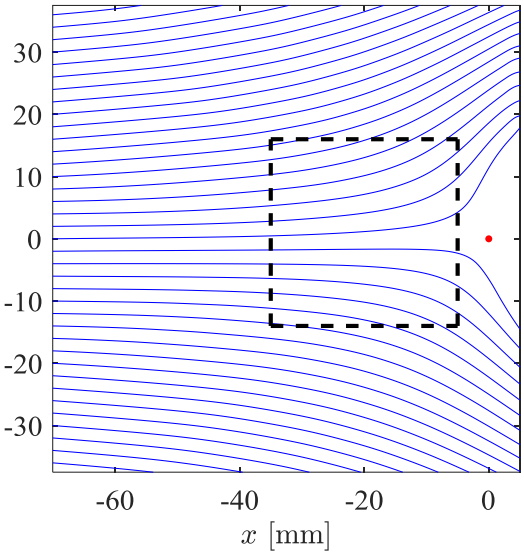

Fig. 4 Streamlines of the reference flow upstream from the airfoil. The dashed black box shows the region where the bubble tracks are considered for Eq. (2). The red dot indicates the approximate location of the stagnation point.

3.3 Freestream flow quality

The flow quality downstream from the modular HFSB generator was measured in the same wind tunnel previously described to investigate the effect of the structure on the flow. The same module configuration shown in Fig. 2 was used, and the measurements were conducted ~5 m downstream from the end of the contraction in the *x*-*z* FOV denoted as FOV2 in Fig. 3. FOV2 was ~30 cm from the floor of the wind tunnel and passed through the centre of the HFSB streamtube. The centre of the streamtube was identified by running the full-scale system while illuminating the cross-section of the streamtube with a laser. The streamtube originates from the ducts and includes the turbulence generated by the blockage of the ducts, nozzles, tubes, and support structure. Note that the nozzles were not being operated during these measurements.

First, the impact of the modular structure on the mean freestream flow was investigated using planar PIV. The same camera and laser system detailed in Section 3.2 was used, but two cameras were implemented here to obtain a wider FOV for capturing more of the spanwise (z) direction in the test section. Two 50-mm lenses with aperture settings of $f/5.6$ were used to obtain a stitched FOV of 197×590 mm^2 with a resolution of 246 μm/pix within FOV2. A laser sheet with a thickness that varied from 1 to 2 mm due to divergence used to

illuminate FOV2. Sets of 2000 double-frame images were collected at 200 Hz for ten freestream velocities ranging from 3.1 to 29.6 m/s, both with and without the modular HFSB generator in the settling chamber of the wind tunnel. DaVis 8.4 (LaVision GmbH) was again used to process the images. The image sets were preprocessed by subtracting the ensemble minimums and then normalized with the ensemble averages. A sum-of-correlation algorithm (Meinhart et al. 2000) was applied using 128×128-pixel (31.5×31.5-mm) Gaussian interrogation windows with 75% overlap to obtain mean velocity fields.

The freestream velocity fluctuation in the centre of FOV2 was measured using a hotwire probe (Custom Hot Wires). Velocity measurements at 20 kHz were recorded over 10 seconds for the same range of freestream velocities mentioned above, with and without the modular structure in the settling chamber of the wind tunnel. The mean velocity fields from PIV were used to calibrate the hotwire probe by fitting a least-squares third-order polynomial to the hotwire voltage signals. The turbulence intensity of the freestream flow was then calculated as the root-mean-square of the fluctuating component of velocity divided by the mean.

4 Results and discussion

4.1 Nozzle production maps

Various production regimes for orifice-type HFSB nozzles were identified by Faleiros et al. (2019). The two primary classifications are bubbling and jetting, under which there are other sub-classifications. Bubbling describes when bubbles form within the nozzle or the orifice, while jetting describes bubble formation external to the nozzle via a jet of He and BFS. Bubble production in each regime is further characterized based on whether the resulting HFSBs are monodisperse or polydisperse. Sample shadow visualizations of monodisperse bubbling, polydisperse bubbling, monodisperse jetting, and polydisperse jetting are presented in Fig. 5.

Several undesirable production regimes are also possible for some nozzle input parameter combinations. Merging, shown in Fig. 5, describes when singly formed bubbles merge into adhered pairs shortly after formation, resulting in undesirable bubble geometry. Satellite formation (through both bubbling and jetting) describes when two distinct populations of bubbles with different mean diameters form simultaneously. The result is a highly bimodal distribution of bubble sizes, i.e. bubbles with two different sets of properties, which is also not ideal for tracers. Attached satellite bubbling refers to when satellite bubbles form attached to the primary bubbles. This type of satellite formation will not result in a bimodal size or time response distribution because each bubble will be similar in size and the overall geometry is still spherical. Sample visualizations of the three satellite formation cases are presented in Fig. 5. Note that the undesirable production regimes mentioned above are often unstable, and have the tendency to transition between one another at a single operating condition. This will be referred to as regime switching.

Following the work of Faleiros et al. (2019), four general umbrella production regimes are defined here to simplify the study of HFSB production using qualitative maps. Moving forward, bubbling will be used to describe monodisperse bubbling, polydisperse bubbling, and attached satellite bubbling in the absence of regime switching. Polydisperse bubbling will result in a wider distribution of diameters, but this regime is rare in the present data and is therefore included in bubbling for simplicity. Attached satellite bubbling is included in bubbling because the resulting bubbles remain monodisperse with a generally spherical shape. Jetting will refer to both monodisperse and polydisperse jetting. Transitional refers to operation that intermittently switches between bubbling and jetting. Finally, atypical production will be used to refer to bubble formation that results in undesirable geometry or two distinct populations of bubbles. Merging, satellite bubbling, and satellite jetting therefore fall under atypical production. All operating points that feature regime switching to one of these undesirable production regimes fall under atypical production as well.

The four umbrella regimes described above have been used to form qualitative production maps for each of the considered nozzle cases: vertical operation of Nozzle 1, Nozzle 2, and Nozzle 3, and horizontal operation of Nozzle 3. The production maps are presented in Fig. 6. No attempt to interpolate or form contours of the results has been made to maintain the actual resolution of the production maps. Despite their coarseness, the maps provide insight into how the production regimes change with input parameters, internal geometry, and operating orientation.

First considering vertical operation, it is evident that increasing $\dot{V}_{\mathrm{BFS}}$ into each nozzle decreases the tendency of the nozzles to operate in the jetting

regime. This effect is significantly more pronounced for Nozzle 2 and Nozzle 3. These two nozzles also experience an increase in the ability to operate in the bubbling regime and a decrease in the ability to operate at higher $\dot{V}_{\mathrm{Air}}$ when $\dot{V}_{\mathrm{BFS}}$ is increased. These trends are accompanied by a movement of the bubbling-jetting transition front to the right on the maps, i.e. in the direction of increasing $\dot{V}_{\mathrm{He}}$. This trend is not visible for Nozzle 1, the map for which appears relatively static with increasing $\dot{V}_{\mathrm{BFS}}$. For all three nozzles, low $\dot{V}_{\mathrm{Air}}$ and $\dot{V}_{\mathrm{He}}$ (the bottom left corner of each map) are associated with operating in the bubbling regime, while high $\dot{V}_{\mathrm{Air}}$ and $\dot{V}_{\mathrm{He}}$ (the top right corner of each map) are associated with the jetting regime. This agrees with intuition because high flowrates of air and He are likely to carry the BFS filament out of the nozzle during operation. Finally, high $\dot{V}_{\mathrm{BFS}}$ seems to be associated with an increase in atypical bubble production. In general, it appears that internal nozzle geometry has a large impact on the production regimes. Moreover, the maps for Nozzle 1 reveal that nearly all the operating cases considered by Gibeau and Ghaemi (2018) were in the jetting regime. This will be discussed more in the following sections.

Considering horizontal operation of Nozzle 3 (Fig. 6d), it is evident that the nozzle does not perform well as stable operation was not achieved for most of the operating points. The ill operation seems to be associated with BFS buildup within the nozzle, and this is corroborated by the fact that performance gets worse with increasing $\dot{V}_{\mathrm{BFS}}$. It seems that vertical operation allows for BFS drainage and assists the axisymmetry of the three concentric flows within the nozzle, which may be disrupted by gravity in the horizontal position due to the relative densities of the three operating fluids. Despite this, the sparse maps reveal that the bubbling-jetting transition front of Nozzle 3 is shifted in the direction of decreasing $\dot{V}_{\mathrm{He}}$ on the maps (left) when operating orientation is changed from vertical to horizontal. This is the same effect that can be seen when $\dot{V}_{\mathrm{BFS}}$ is reduced for vertical operation of Nozzle 2 and Nozzle 3. The maps of Fig. 6c,d

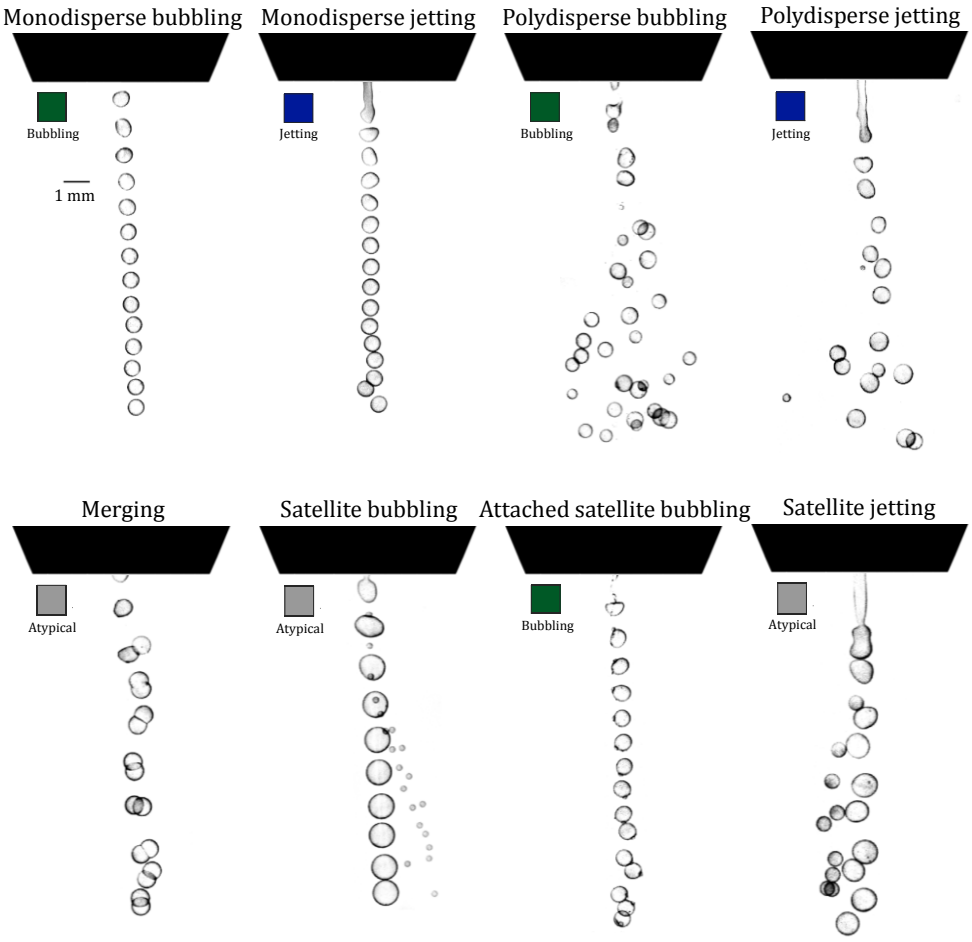

Fig. 5 Shadow visualizations of the various production regimes observed for the current nozzle designs. The colors and labels associated with each regime indicate the umbrella categories bubbling, jetting, and atypical used in Fig. 6.

therefore suggest that operating orientation impacts the production regimes of the current nozzle.

Bubbling is the most desirable production regime because the resulting bubbles are spherical and monodisperse. It is therefore evident from Fig. 6 that Nozzle 3 (vertical) has the best performance overall since it operates in the bubbling regime for the largest number of input combinations. When Nozzle 3 is compared to Nozzle 1, it is evident that the modification to internal geometry has greatly improved the operation of the nozzle. We postulate that the extended bubbling regime is a result of the improved axisymmetry of air flow within the nozzle. Bubble formation within the nozzle, i.e. bubbling, requires that the outer flow of air surrounds and pinches the filament of He and BFS to form individual bubbles. Presumably, this is possible at higher $\dot{V}_{\mathrm{Air}}$ and $\dot{V}_{\mathrm{He}}$ for Nozzle 3 because of the improved axisymmetry of the internal flows. The same is likely true for Nozzle 2, but to a lesser extent as the geometric modification was not as extreme but aids the internal flow in the same manner.

The production maps reported by Faleiros et al. (2019) for a horizontal nozzle reveal similarities when compared to the present maps. For example, they also show that increasing $\dot{V}_{\mathrm{BFS}}$ results in an increased tendency to bubble and a decreased tendency to jet, and their bubbling-jetting transition front also corresponds to a division between the lower left (low $\dot{V}_{\mathrm{Air}}$, low $\dot{V}_{\mathrm{He}}$) and upper right (high $\dot{V}_{\mathrm{Air}}$, high $\dot{V}_{\mathrm{He}}$) regions of their maps. However, their maps feature large regions of polydisperse bubbling for inputs that produced monodisperse bubbling here. Moreover, their nozzles operate for air inputs up to at least $\dot{V}_{\mathrm{Air}} = 2.5$ L/min, which was not possible using the present nozzle designs. Finally, their nozzles appear to function well when oriented horizontally, while the present nozzles do not. These comparisons further strengthen the present finding that internal nozzle geometry is a critical factor for nozzle performance. Moving forward, only vertical nozzle operation will be considered for analysis within this work due to the poor operation of the present nozzles in the horizontal operating orientation.

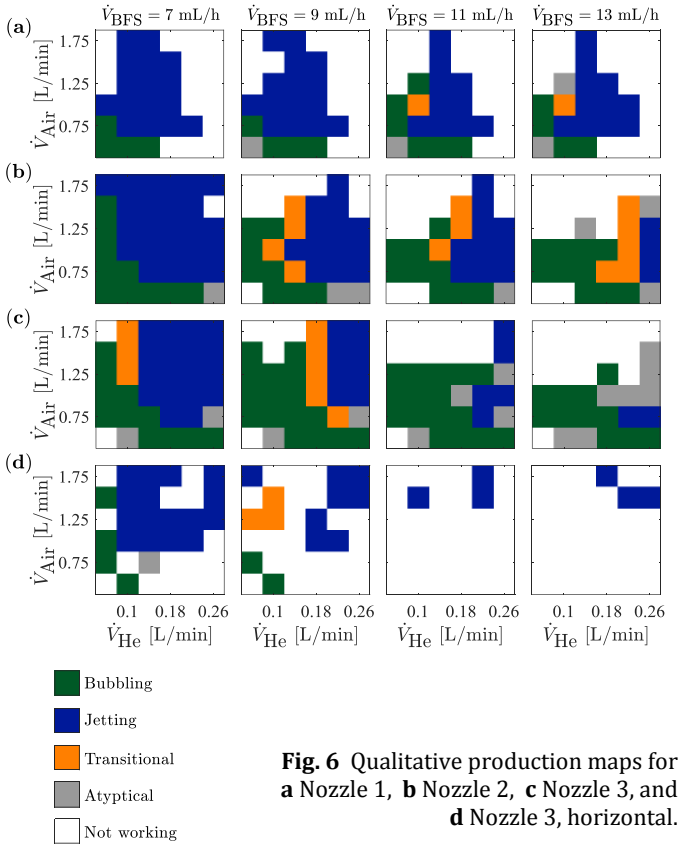

Fig. 6 Qualitative production maps for **a** Nozzle 1, **b** Nozzle 2, **c** Nozzle 3, and **d** Nozzle 3, horizontal.

4.2 Size distributions

Following Section 3.1, the distribution of bubble diameters (d) has been determined for all operating points that exhibit bubbling, jetting, or transitional behaviour. A sample distribution from each of these three regimes is provided in Fig. 7. The horizontal axis scales between the distributions in the figure have been held constant to facilitate comparison. Bubbling (monodisperse) produces bubbles with a narrow, unimodal distribution that is slightly left-skewed. The bubbling sample in Fig. 7 features a standard deviation that is 2% of the mean. In contrast, jetting (polydisperse) produces bubbles with a wide range of diameters. The sample distribution for jetting is bimodal and features a standard deviation that is 26% of the mean. Transitional production is characterized by regime switching between bubbling and jetting and this is visible in the sample distribution in Fig. 7, where the distribution seems to be a combination of the narrow bubbling distribution and the wide, bimodal jetting distribution, caused by intermittent switching between bubbling and jetting during operation. The sample distributions within Fig. 7 are representative of the large majority of bubbling, jetting, and transitional cases observed in the present data.

The mean diameters ($\bar{d}$) and normalized standard deviations ($\sigma_d/\bar{d}$) for all bubbling, jetting, and transitional cases for the first three values of $\dot{V}_{\mathrm{BFS}}$ have been plotted as maps in Fig. 8, where the regions outlined in black denote the bubbling regime. The maps of $\bar{d}$ for the three nozzles reveal similar trends. In general, increasing $\dot{V}_{\mathrm{He}}$ leads to

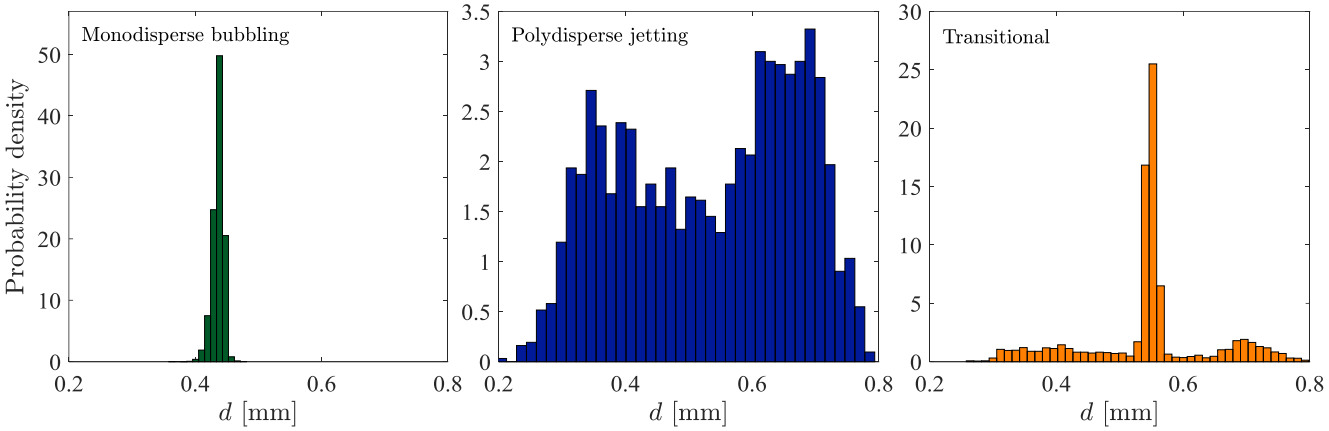

Fig. 7 Sample histograms of bubble diameter (d) for production in the bubbling, jetting, and transitional regimes. All samples are from vertical operation of Nozzle 3.

larger bubbles, while increasing $\dot{V}_{\mathrm{Air}}$ leads to smaller bubbles. It is also evident that there is no clear effect on $\bar{d}$ due to the transition of production regimes. However, the regimes directly affect the standard deviations (σ_d) associated with the resulting diameter distributions. As is evident in Fig. 8, the bubbles formed via the bubbling regime (outlined in black) generally have a standard deviation that is less than 5% of the mean. A few exceptions occur for the cases of polydisperse bubbling, which are quite rare in the current data set. In contrast, bubble distributions formed via the jetting regime have standard deviations that extend upwards of 30% of the mean. As is visible in Fig. 8, the largest $\sigma_d/\bar{d}$ are found for jetting cases with low $\dot{V}_{\mathrm{Air}}$ and high $\dot{V}_{\mathrm{He}}$. The jetting cases with very small $\sigma_d/\bar{d}$ only occur for monodisperse jetting, which is also very rare. Transitional cases produce distributions with $\sigma_d/\bar{d}$ that is somewhere between those associated with bubbling and jetting and depends on the relative switching between the two regimes.

Faleiros et al. (2019) presented a scaling law for $\bar{d}$ as a function of the input parameters and the nozzle orifice diameter (d_{o}). This law was constructed using both empirical observations and theoretical considerations, and it will be briefly described here. The authors observed that the bubble production rate scales linearly with the ratio of air input and orifice diameter, i.e.:

$$\dot{N} \sim \frac{\dot{V}_{\mathrm{Air}}}{d_{\mathrm{o}}} \tag{3}$$

where $\dot{N}$ is the production rate in bubbles/s. Additionally, ideal production of HFSBs (constant $\bar{d}$ and no He leakage) while neglecting the thickness of the soap film will result in bubbles with a volume of:

$$V_{\mathrm{b}} = \frac{\pi}{6}\bar{d}^3 = \frac{\dot{V}_{\mathrm{He}}}{\dot{N}}. \tag{4}$$

Combining Eq. (3) and (4) above yields:

$$\bar{d} \sim \left(\frac{d_{\mathrm{o}}\dot{V}_{\mathrm{He}}}{\dot{V}_{\mathrm{Air}}}\right)^{1/3}. \tag{5}$$

The above scaling law has been plotted in Fig. 9 to compare across the three considered nozzles, to compare between bubbling and jetting, and to compare with the results from Gibeau and Ghaemi (2018) for various values of $\dot{V}_{\mathrm{BFS}}$ (Nozzle 1 only). Beginning with Fig. 9a, it is evident that there is no apparent difference between the scaling law trends of the three considered nozzles. Moreover, the slope of the overall linear trend visible in the plot agrees well with the slope of the linear fit provided by Faleiros et al. (2019) for the NLR nozzle (Netherlands Aerospace Centre), which features a similar orifice diameter of 1 mm. The scatter of data about the linear trend reveals that the scaling law does not provide a perfect representation of the results. This could potentially stem from measurement uncertainties or the various assumptions involved in its derivation. Considering Fig. 9b, there is also no apparent difference in the scaling law between the bubbling and jetting regimes for the present data set. However, Fig. 9c reveals that the present results differ from those of Gibeau and Ghaemi (2018) for $\dot{V}_{\mathrm{BFS}} = 4, 6, \text{and } 8$ mL/h. The trend for $\dot{V}_{\mathrm{BFS}} = 8$ mL/h is similar to those found in the present results for similar values

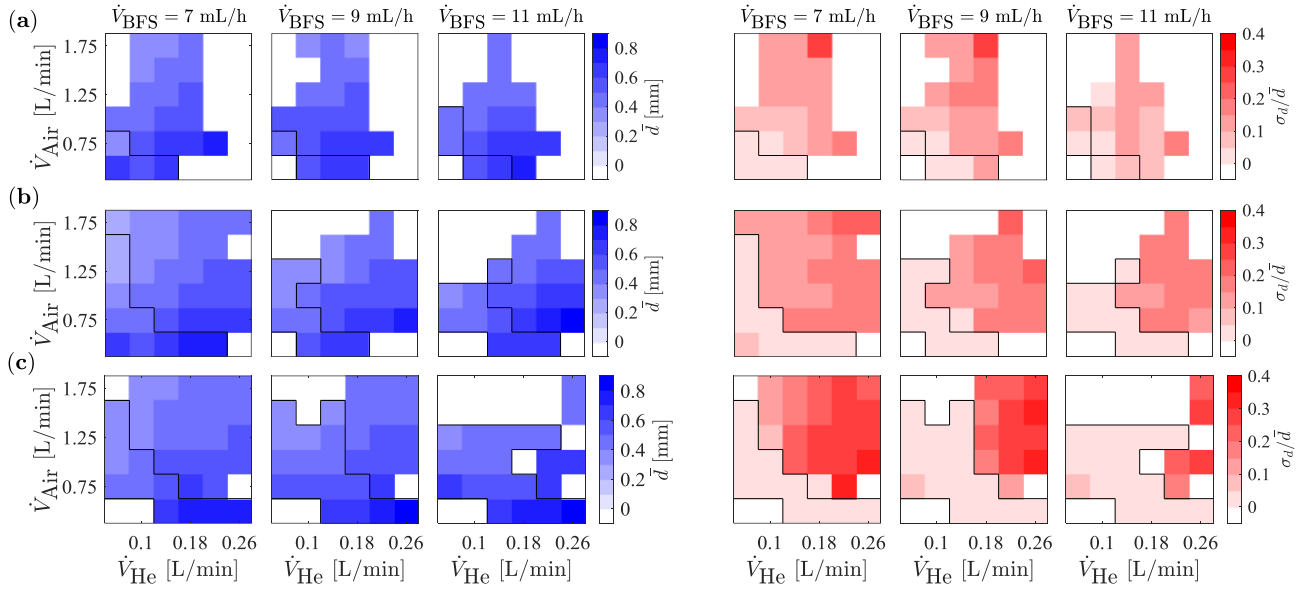

Fig. 8 Maps of mean bubble diameter (left) and the associated normalized standard deviations (right) for **a** Nozzle 1, **b** Nozzle 2, and **c** Nozzle 3, all operated vertically. The black outlines show regions of bubbling.

of $\dot{V}_{BFS}$, and the small difference may be attributable to the multi-nozzle generator used for bubble diameter measurements in their study, in contrast to the single nozzle used here. For $\dot{V}_{BFS} = 4$ and 6 mL/h, the linear trends reduce in slope, revealing that the resulting bubbles are smaller than what the scaling law of Eq. (5) predicts for larger $\dot{V}_{BFS}$. This effect is most pronounced for $\dot{V}_{BFS} = 4$ mL/h. Since these trends show a reduced bubble diameter for the same nozzle inputs, it is likely that He was leaked during the bubble formation process. As discussed in the introduction, Gibeau and Ghaemi (2018) found that their bubble production rates depended on $\dot{V}_{BFS}$. Additionally, Section 4.1 revealed that the nozzles of Gibeau and Ghaemi (2018) were operating primarily in the jetting regime during their experiments. The results plotted in Fig. 9c therefore suggest that operating in the jetting regime with insufficient BFS results in He leakage, as the scaling of $\bar{d}$ reduces as $\dot{V}_{BFS}$ is reduced to low values within the jetting regime. It seems that $\dot{V}_{BFS}$ is limiting under these circumstances. This will be discussed in the context of production rates and time response trends in the following sections.

4.3 Production rates

The bubble production rates ($\dot{N}$) have been determined using Eq. (1) for various operating cases in the bubbling regime to investigate the trends of $\dot{N}$ as a function of the nozzle input parameters. Only monodisperse bubbling operation was considered because Eq. (1) requires an orderly sequence of produced bubbles (see Fig. 5). Nozzle 3 was chosen for this analysis because it exhibits bubbling over the largest extent of input parameters as is evident in Fig. 6. Select results from Faleiros et al. (2019) are included for comparison, and the results of Gibeau and Ghaemi (2018) are investigated in parallel to demonstrate the differences between bubbling and jetting, as Fig. 6a revealed that the production rate analysis of Gibeau and Ghaemi (2018) using Nozzle 1 was conducted for operating points primarily in the jetting regime. Note that the method of calculating $\dot{N}$ used in their study is different than the one used here. It involved counting bubbles in a volume illuminated by a laser sheet downstream from their HFSB generator. This method is prone to overestimation because it is difficult to know the effective thickness of the illuminated volume in which the counting is taking place. Regardless, the trends remain valid, and it is the trends that will be compared in the present analysis.

The results for $\dot{N}$ are plotted in Fig. 10 as a function of the three input parameters and compared to those of Faleiros et al. (2019) and Gibeau and Ghaemi (2018). The results as a function of $\dot{V}_{Air}$ reveal two different trends for the bubbling (a) and jetting (b) regimes. In the bubbling regime, $\dot{N}$ increases sharply in a super-linear fashion with increasing $\dot{V}_{Air}$, while $\dot{V}_{Air}$ does not seem to affect $\dot{N}$ during jetting. When $\dot{V}_{He}$ is increased, $\dot{N}$ increases for

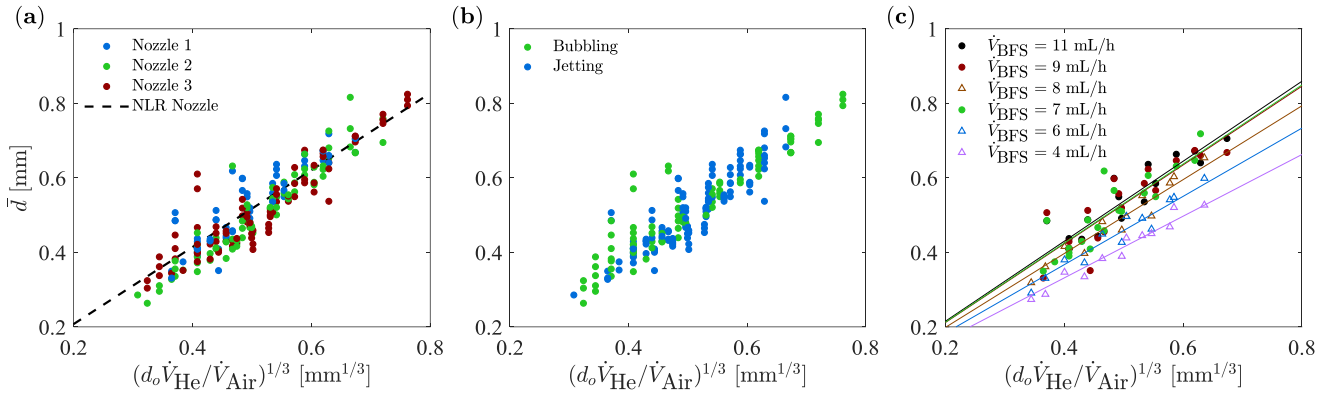

Fig. 9 Scaling of mean bubble diameter following Eq. (5) for **a** all three nozzles compared to the linear fit of Faleiros et al. (2019) for the NLR nozzle, **b** all three nozzles split into bubbling and jetting cases, and **c** Nozzle 1 compared to the results from Gibeau and Ghaemi (2018) for 8 nozzles, which are shown using triangles.

bubbling and decreases for jetting, revealing opposite trends. When $\dot{V}_{BFS}$ is increased, a small reduction of $\dot{N}$ is observed in the bubbling regime, while a sharp, linear increase is observed for jetting. All present $\dot{N}$ trends in Fig. 10a for the bubbling regime exhibit similar behavior as those reported by Faleiros et al. (2019).

In the bubbling regime, $\dot{N}$ is dominated by $\dot{V}_{Air}$, while $\dot{V}_{He}$ and $\dot{V}_{BFS}$ offer smaller effects. Since $\bar{d}$ decreases with increasing $\dot{V}_{Air}$, the mechanism behind the sharp $\dot{N}$ increase seems to be the production of smaller bubbles in greater numbers. Considering the jetting results from Gibeau and Ghaemi (2018), $\dot{N}$ is dominated by $\dot{V}_{BFS}$, while $\dot{V}_{Air}$ has a negligible effect and $\dot{V}_{He}$ results in a small production decrease. Fig. 9 revealed that $\bar{d}$ is not significantly affected when BFS is provided in sufficient amounts, but that insufficient BFS suggests He leakage for the jetting regime. The mechanism behind the sharp $\dot{N}$ increase in the jetting regime with increasing $\dot{V}_{BFS}$ may therefore be the utilization of excess He that is lost when there is insufficient BFS. The production regime maps of Fig. 6 show that increasing $\dot{V}_{BFS}$ results in the movement of the bubbling-jetting transition front in the direction of increasing $\dot{V}_{He}$. This would mean that a given operating point ($\dot{V}_{Air}$, $\dot{V}_{He}$) can switch from jetting to bubbling when $\dot{V}_{BFS}$ is increased. This behaviour, when coupled with the possible He leakage in the jetting regime, suggests that jetting could be associated with He leakage until sufficient BFS is provided, at which point production switches to the bubbling regime. Further investigation is necessary to confirm this. Moreover, the relatively small sample of results taken from Gibeau and Ghaemi (2018) may not be representative of all jetting behaviour.

4.4 Time responses

The time response (τ) of the HFSBs was estimated using the same method employed by Scarano et al. (2015), Gibeau and Ghaemi (2018), and Faleiros et al. (2018, 2019). The details of this experiment are provided in Section 3.2. All operating points in the bubbling regime of Nozzle 3 with mean diameters between 0.3 and 0.6 mm were considered, resulting in 24 cases total. A sample distribution of τ is shown in Fig. 11 with a normal distribution fit for comparison. The distribution was obtained for inputs of $\dot{V}_{Air}$ = 1.25 L/min, $\dot{V}_{He}$ = 0.10 L/min, and $\dot{V}_{BFS}$ = 9 mL/h, and can be seen to be approximately normally distributed. The remaining distributions are similar to this sample.

Faleiros et al. (2019) showed that the time response of a HFSB depends on the ratio of BFS and He inputs. Assuming the ideal case, that there is no BFS spillage or He leakage, the conservation of mass can be employed to obtain:

$$\rho_b V_b \dot{N} = \rho_{He}\dot{V}_{He} + \rho_{BFS}\dot{V}_{BFS} \quad (6)$$

where the densities of the bubble, He, and BFS are denoted as ρ_b, ρ_{He}, and ρ_{BFS}, respectively. Eq. (4) can be combined with Eq. (6) above to obtain:

$$\rho_b = \rho_{He} + \rho_{BFS}\frac{\dot{V}_{BFS}}{\dot{V}_{He}}. \quad (7)$$

The theoretical density of a HFSB, and also its time response, is therefore a linear function of $\dot{V}_{BFS}/\dot{V}_{He}$.

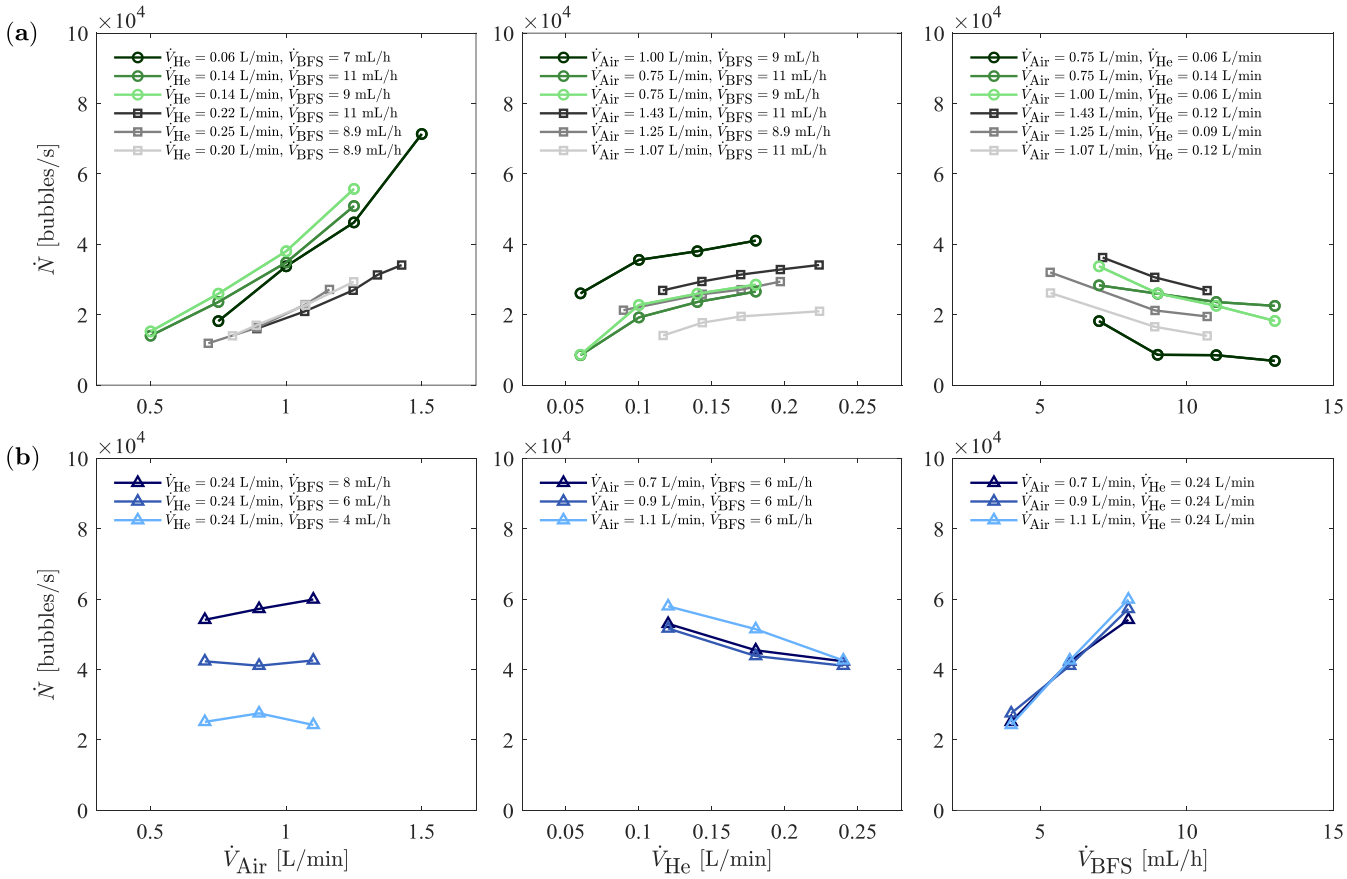

Fig. 10 Production rate ($\dot{N}$) trends as a function of air, He, and BFS inputs. **a** The present monodisperse bubbling results (circles) from the shadowgraphy measurements of Nozzle 3 compared to select results of Faleiros et al. (2019) (squares). **b** The jetting results from Gibeau and Ghaemi (2018).

This linear relation is approximated here using $\dot{V}_{He}/\dot{V}_{BFS}$.

The relationship between the mean time response ($\bar{\tau}$) and $\dot{V}_{He}/\dot{V}_{BFS}$ is plotted in Fig. 12 for the 24 bubbling cases measured here in comparison to the results of Gibeau and Ghaemi (2018) and Faleiros et al. (2019). The lines in the plot are least-squares linear fits of the corresponding data, and the grey dashed crossing represents neutral buoyancy ($\rho_b = \rho_{Air}$) with zero response time based on the ideal case of Eq. (7), i.e. the linear fit should pass through the grey crossing for the ideal case. The present bubbling results in Fig. 12 reveal that a linear relationship is satisfied, but the $\bar{\tau} = 0$ crossing occurs prior to the point predicted by theory. This is most likely due to BFS spillage during the bubble formation process, as the ratio $\dot{V}_{He}/\dot{V}_{BFS}$ would be larger if BFS spillage was accounted for. The $\bar{\tau} = 0$ crossing point for the present bubbling results occurs at $\dot{V}_{He}/\dot{V}_{BFS} \approx 750$, which is different than the value reported by Faleiros et al. (2019) as is visible in Fig. 12. This suggests that neutral buoyancy is achieved at a different input ratio for different HFSB generators. It also seems that some degree of BFS spillage during operation in the bubbling regime may be a normal side effect of using the current nozzle designs, as the present results and those of Faleiros et al. (2019) both show $\dot{V}_{He}/\dot{V}_{BFS}$ smaller than the ideal value at $\bar{\tau} = 0$. It is possible that optimizing nozzle geometry could lead to a nozzle capable of bubbling without spilling BFS.

In contrast to the bubbling results, the results in Fig. 12 from Gibeau and Ghaemi (2018) reveal linear fits that cross $\bar{\tau} = 0$ after the theoretically ideal point. This suggests He leakage during bubble formation instead of BFS spillage and is therefore in agreement with the mean diameter scaling (Fig. 9) and production rate (Fig. 10) results, which also suggested He loss in the results of Gibeau and Ghaemi (2018). Moreover, the linear trends move towards the ideal crossing point as $\dot{V}_{BFS}$ is increased, indicating that more He is utilized as more BFS is made available. This supports the notion that operating in the jetting regime with insufficient BFS

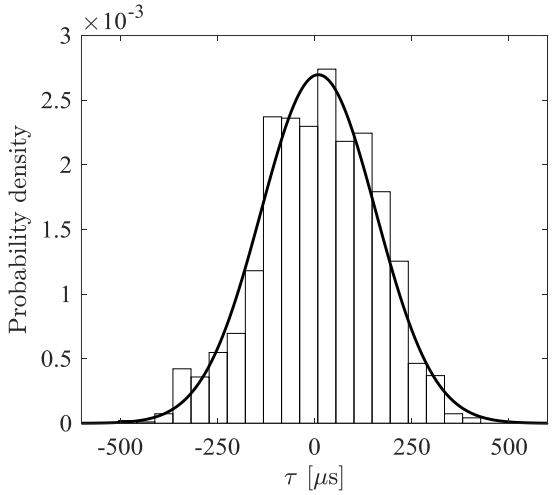

Fig. 11 Sample time response distribution with a normal distribution fit for comparison.

results in He leakage, with BFS acting as a sort of limiting reagent.

Finally, the standard deviations associated with the time responses (σ_τ) for the 24 bubbling cases are plotted in Fig. 12. The plot reveals that σ_τ is relatively constant at $\sigma_\tau \approx 150$ µs for all cases considered, although more variability is observed at lower $\dot{V}_{\mathrm{He}}/\dot{V}_{\mathrm{BFS}}$. These values agree with the standard deviation of the optimal case reported by Gibeau and Ghaemi (2018) for an 8-nozzle system ($\sigma_\tau = 171$ µs) and are roughly 3 times larger than those reported by Faleiros et al. (2018, 2019) for a single nozzle. The larger standard deviations of the present results may be due to difficulties ensuring equal flow rates to each nozzle in the present multi-nozzle system, or slight differences between the 3D-printed nozzles. This could have resulted in each nozzle producing bubbles with slightly different distributions, or even some nozzles producing polydisperse bubbles during operation. The similar σ_τ reported here (bubbling) in comparison to the result of Gibeau and Ghaemi (2018) (jetting) suggests that whether the nozzles are bubbling or jetting does not significantly affect the width of the time response distribution (i.e. standard deviation) for a multi-nozzle system. This is also visible in the results of Faleiros et al. (2019), who concluded that the deviations in τ may be a result of variations in the thickness of the soap film, which would in turn affect bubble density. The variations in soap film thickness may therefore be more important than bubble diameter for regulating σ_τ.

4.5 Effective tracing fidelity for PIV

Monte Carlo simulations have been employed to help answer a question posed in the introduction: how does the effective time response distribution of produced bubbles vary during applications of PIV? When PTV is applied to HFSBs, conclusions regarding tracing fidelity from the directly measured time response distribution apply because only a single bubble is considered at once, and a single bubble could have a time response that falls anywhere on the measured distribution. In contrast, PIV correlates groups of bubbles each with a different time response, which brings up the question of the effective time response of the correlated group. If the PIV cross-correlation applies an equal weighting to each bubble considered, then using the average time response of that group is a good estimate of the effective time response associated with that cross-correlation. However, larger bubbles may be brighter, and the cross-correlation will be biased towards these brighter bubbles with a larger intensity count. This could pose an issue for the assumption that the average

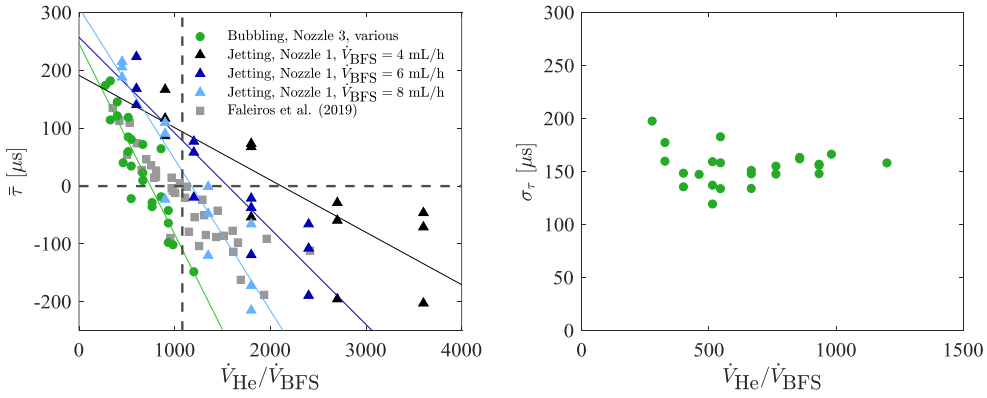

Fig. 12 Mean time responses ($\bar{\tau}$) and the associated standard deviations (σ_τ) as a function of the ratio of He and BFS inputs. The Nozzle 1 results (triangles) are from Gibeau and Ghaemi (2018). The grey dashed crossing represents the location where the linear trend should pass for the ideal case. The data of Faleiros et al. (2019) is included for comparison.

time response of the group adequately represents the cross-correlation. But, as Faleiros et al. (2019) demonstrated, the time response of a HFSB is dictated by more than just its diameter. They found that the time response standard deviations associated with bubbles produced in the jetting regime were smaller on average than those produced by bubbling, despite the larger deviation in bubble sizes associated with jetting. This reveals that that the bias of the cross correlations towards larger, brighter bubbles does not necessarily indicate a bias in time response.

Assuming that the effective time response of a group of particles is the mean time response of that group, very large groups of particles will have an effective time response that approaches the mean of the measured distribution. This value will be $\bar{\tau} = 0$ (perfect tracing) when the nozzle inputs are selected to achieve bubbles that are neutrally buoyant on average. However, it is recommended that applications of PIV correlate at least 10 particles per interrogation window (Keane and Adrian 1992), which is not enough to average out the effect of a broad distribution. Regardless, some narrowing of the effective time response distribution is expected, and this is estimated here.

We first assume normally distributed particle time responses with a mean of $\bar{\tau} = 0$ and a standard deviation of $\sigma_\tau = 1$ as the starting distribution. This assumption is reasonable since both Gibeau and Ghaemi (2018) and Faleiros et al. (2018) showed that HFSB time response distributions were approximately normally distributed. This is also the case for the present time response distributions, a sample for which is presented in Fig. 11 with a normal distribution fit for comparison. We then employ the previous assumption that the effective time response of a group of particles in a given interrogation region (τ') is the mean time response of that group. A select number of particles are randomly simulated using the starting time response distribution defined above and their values are averaged to obtain τ'. This value is then added to the new distribution. This operation has been performed $N = 10^6$ times for varying numbers of particles per interrogation region (PPIR) to form converged distributions of τ'. The effective standard deviations associated with these distributions ($\sigma_{\tau'}$) are then computed and normalized by the standard deviation of the original distribution (σ_τ). The results have been plotted in Fig. 13. When PPIR = 1, the starting distribution is reproduced, resulting in $\sigma_{\tau'}/\sigma_\tau = 1$. As PPIR increases, $\sigma_{\tau'}$ exhibits a steep decline that asymptotically approaches $\sigma_{\tau'}/\sigma_\tau = 0$. This is

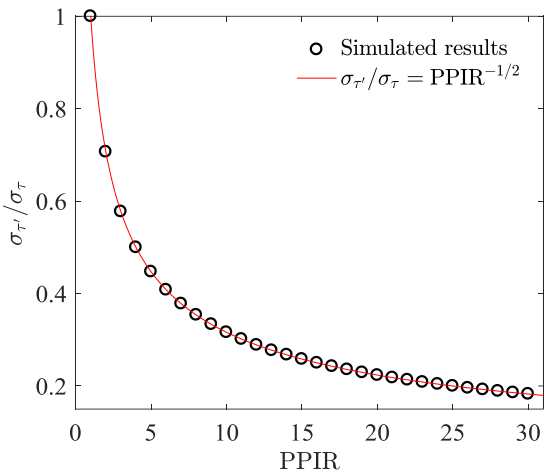

Fig. 13 Standard deviation of the effective time response distribution ($\boldsymbol{\sigma_{\tau'}}$) as function of the number of particles per interrogation region (PPIR).

expected because τ' approaches 0 as the number of considered particles becomes very large as previously discussed. As is visible in the figure, the trend obeys the power law $\sigma_{\tau'}/\sigma_\tau = \mathrm{PPIR}^{-1/2}$. When PPIR = 10, which is the recommended minimum for PIV, we obtain $\sigma_{\tau'}/\sigma_\tau = 0.32$. For PPIR = 20, the result is $\sigma_{\tau'}/\sigma_\tau = 0.22$. This suggests a 3- to 5-fold improvement in tracing fidelity when groups of 10 to 20 particles are correlated, which is common for applications of PIV.

The power law demonstrated in Fig. 13 can be used for the design of a HFSB experiment. First, we assume that the distribution of time responses is normally distributed with a mean of zero, which can be ensured using the ratio $\dot{V}_{\mathrm{He}}/\dot{V}_{\mathrm{BFS}}$ as was demonstrated in Section 4.4 and by Faleiros et al. (2019). We then employ the *Z*-score property of the normal distribution: that a chosen percentage of the distribution is *Z* standard deviations from the mean. This *Z*-score is used to select the proportion of HFSBs that will be accurate within design specification, e.g. 95% for $Z = 2$ and 99.7% for $Z = 3$. Finally, the recommendation that the time response of a particle be an order of magnitude smaller than the time scale it is measuring is invoked (Tropea et al. 2007). We can then define the minimum time scale τ_{min} that can be accurately measured using HFSBs with a time response standard deviation σ_τ such that a chosen percentage of the particles fall within Z standard deviations of the mean for a given PPIR:

$$\tau_{\mathrm{min}} = \frac{10Z\sigma_\tau}{\sqrt{\mathrm{PPIR}}}. \tag{8}$$

For example, using the present results, we can operate at $\dot{V}_{\mathrm{He}}/\dot{V}_{\mathrm{BFS}} = 750$ to obtain bubbles that are neutrally buoyant on average with $\sigma_\tau = 150$ µs. If the minimum recommendation for PIV is employed (PPIR = 10) and we want 95% of the particles produced by the system to be accurate ($Z = 2$), we arrive at a minimum measurable time scale of $\tau_{\mathrm{min}} = 949$ µs. This value can be used in the experimental design phase to ensure that measurements conducted using HFSBs will not be significantly affected by the tracing fidelity of the bubbles.

4.6 Full-scale implementation

The maximum freestream deviation from the mean and the freestream turbulence intensities have been measured using PIV and hotwire anemometry as described in Section 3.3. Ten freestream velocities ranging from 3.1 to 29.6 m/s have been considered with and without the modular HFSB generator placed in the settling chamber of the wind tunnel as shown schematically in Fig. 3, and the results are shown in Fig. 14. The plot reveals that the largest deviation from the mean without the structure is 1.1% and occurs at the lowest freestream velocity. This larger deviation is due to poor flow quality at low velocities, which is a characteristic of the present wind tunnel. At 6 m/s or above, the maximum freestream deviation from the mean is 0.7%. The maximum value increases to 1.9% when the HFSB structure is added to the settling chamber of the wind tunnel. As is evident in Fig. 14, the largest deviations from the mean occur in the mid-range of velocities considered (~10-20 m/s), and the HFSB structure does not seem to impose a noticeable deficit at the three highest velocities. The figure also shows the freestream turbulence intensities for the same cases, which can be seen to follow similar trends. Specifically, there is poor flow quality at the lowest freestream velocity and no effect at the three highest velocities. Without the HFSB structure, all freestream turbulence intensities are 0.6% or lower. These values increase by at most 0.3% when the HFSB structure is added to the settling chamber of the wind tunnel at freestream velocities of 6 m/s or greater. A larger increase of 0.5% is observed for the lowest freestream velocity. We emphasize that these measurements only capture the effect of the modular structure on the flow and were conducted without flow in the nozzles as mentioned in Section 3.3. They therefore do not account for any turbulence that may be generated by the jet at the exit of each nozzle.

The full-scale modular HFSB system shown in Fig. 2 has been used to demonstrate the seeding of a 3D-PTV experiment in the present wind tunnel. A total of 4 modules each featuring 12 nozzles (Nozzle 3) were employed. The wake of a half-scale, square-back Ahmed body was recorded at 10 m/s. A sample image from the experiment is provided in Fig. 15, which shows an illuminated volume of approximately 20,000 cm^3. A density of 0.02 particles per pixel (ppp) was obtained.

5 Summary and conclusions

This work investigated several aspects associated with using a full-scale HFSB generator for wind tunnel applications. Shadowgraphy, PTV, PIV, hotwire anemometry, and Monte Carlo simulations were used to investigate production regimes, bubble size, production rates, time responses, and the flow quality downstream from a full-scale generator. The present results in tandem with results from past investigations lead to various conclusions. The primary results pertaining to the use and design of HFSB generators are summarized here.

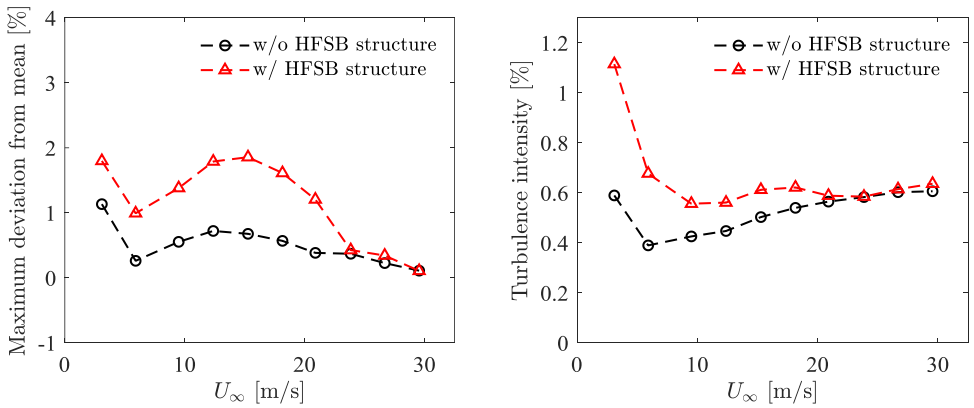

Fig. 14 Maximum freestream deviation from the mean (from PIV) and freestream turbulence intensities (from hotwire anemometry) with and without the modular HFSB structure in the settling chamber of the wind tunnel.

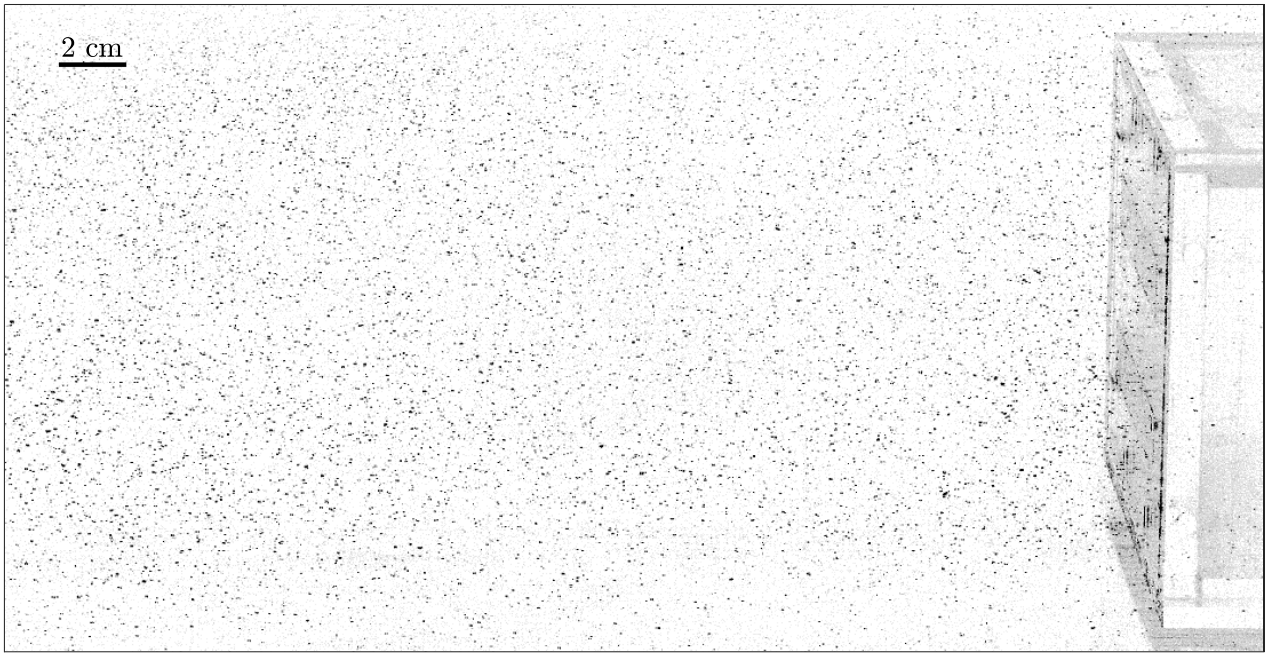

Fig. 15 Sample image showing HFSB seeding in the wake of a half-scale, square-back Ahmed body with a 19.5×14.4 cm^2 back face. The experiment was conducted at 10 m/s using 48 nozzles (Nozzle 3), resulting in 0.02 ppp. A volume of roughly 20,000 cm^3 is illuminated in the image.

(i) Modifications to internal nozzle geometry directly affect nozzle performance. This includes the production regimes that the nozzle operates in for a given combination of input parameters and the overall range of input combinations for which a nozzle will function. This is important from the perspective of maximizing production rates from a single nozzle. A nozzle that operates in the bubbling regime at high air and He inputs will be able to produce more bubbles overall because both air and He dictate production rates in this regime.

(ii) The input flow of BFS should be properly selected for a given HFSB nozzle. The present results show that small $\dot{V}_{\mathrm{BFS}}$ increases the tendency of a nozzle to jet, while large $\dot{V}_{\mathrm{BFS}}$ leads to an increased occurrence of atypical production (merging, satellite bubbling, and satellite jetting). Moreover, comparison of the present Nozzle 1 results with those of Gibeau and Ghaemi (2018) for the same nozzle suggests that operating in the jetting regime with low BFS may result in He leakage during bubble formation, thus reducing bubble production rates overall.

(iii) The mean time response of the bubbles produced by a HFSB generator scales linearly with $\dot{V}_{\mathrm{He}}/\dot{V}_{\mathrm{BFS}}$. However, the exact ratio that produces bubbles that are neutrally buoyant on average may vary for different HFSB generators. This variance could be a function of the spilled BFS and leaked He during bubble formation, which could be different depending on the generator. The ratio that produces bubbles that are neutrally buoyant on average should therefore be determined for each individual HFSB generator so that ideal operating inputs for experiments can be established.

(iv) Assuming that a HFSB generator is operated to produce bubbles that are neutrally buoyant on average, the standard deviation of time responses associated with the bubbles determines the minimum time scale that the bubbles can be used to accurately measure. Moreover, the spatial averaging effect associated with correlating groups of bubbles reduces the effective standard deviation of the time response distribution by a factor of $\mathrm{PPIR}^{-1/2}$, where PPIR is the number of particles per interrogation region. The minimum measurable time scale is therefore a function of the time response standard deviation, the number of PPIR, and the chosen proportion of bubbles/particles produced by a generator that are to accurately track the minimum time scale. Eq. (8) provides a means of calculating this minimum time scale for experimental design purposes.

(v) Placing a full-scale HFSB generator in the settling chamber of a wind tunnel induces measurable changes in the downstream flow quality due to the physical blockage of the nozzle support structure. For the present modular system, the maximum change in freestream uniformity was 1.2% of the mean, and the maximum increase in the freestream turbulence intensity was 0.3% for freestream velocities of 6 m/s or greater. While these differences are relatively small, they should be considered when designing experiments that will make use of a full-scale HFSB generator.

Acknowledgements

We acknowledge the support of the Natural Sciences and Engineering Research Council of Canada (NSERC) [Alexander Graham Bell Canada Graduate Scholarship – Doctoral]. We also thank Dr. Markus Raffel of the German Aerospace Centre (DLR) for insightful discussions regarding nozzle design, and Prof. David Wood of the University of Calgary for lending the hotwire anemometry system used in this study.

References

Bosbach J, Kühn M, Wagner C (2009) Large scale particle image velocimetry with helium filled soap bubbles. Exp Fluids 46:539-547

Caridi GCA, Ragni D, Sciacchitano A, Scarano F (2016) HFSB-seeding for large-scale tomographic PIV in wind tunnels. Exp Fluids 57:190

Caridi GCA, Sciacchitano A, Scarano F (2017) Helium-filled soap bubbles for vortex core velocimetry. Exp Fluids 58:130

Elsinga GE, Scarano F, Wieneke B, van Oudheusden BW (2006) Tomographic particle image velocimetry. Exp Fluids 41:933-947

Faleiros DE, Tuinstra M, Sciacchitano A, Scarano F (2018) Helium-filled soap bubbles tracing fidelity in wall-bounded turbulence. Exp Fluids 59:56

Faleiros DE, Tuinstra M, Sciacchitano A, Scarano F (2019) Generation and control of helium-filled soap bubbles for PIV. Exp Fluids 60:40

Gibeau B, Ghaemi S (2018) A modular, 3D-printed helium-filled soap bubble generator for large-scale volumetric flow measurements. Exp Fluids 59:178

Hale RW, Tan P, Stowell RC, Ordway DE (1971) Development of an integrated system for flow visualization in air using neutrally-buoyant bubbles. SAI-RR 7107, SAGE ACTION Inc, Ithaca NY

Huhn F, Schanz D, Gesemann S, Dierksheide U, van de Meerendonk R, Schröder A (2017) Large-scale volumetric flow measurement in a pure thermal plume by dense tracking of helium-filled soap bubbles. Exp Fluids 58:116

Jux C, Sciacchitano A, Schneiders JFG, Scarano F (2018) Robotic volumetric PIV of a full-scale cyclist. Exp Fluids 59:74

Keane RD, Adrian RJ (1992) Theory of cross-correlation analysis of PIV images. Appl Sci Res 49:191-215

Kerho MF, Bragg MB (1994) Neutrally buoyant bubbles used as flow tracers in air. Exp Fluids 16:393-400

Kühn M, Ehrenfried K, Bosbach J, Wagner C (2011) Large-scale tomographic particle image velocimetry using helium-filled soap bubbles. Exp Fluids 50:929-948

Meinhart CD, Wereley ST, Santiago JG (2000) A PIV algorithm for estimating time-averaged velocity fields. J Fluids Eng 122:285-289

Müller D, Müller B, Renz U (2001) Three-dimensional particle-streak tracking (PST) velocity measurements of a heat exchanger inlet flow. Exp Fluids 30:645-656

Raffel M, Willert CE, Scarano F, Kähler C, Wereley ST, Kompenhans J (2018) *Particle Image Velocimetry: A Practical Guide*. Springer, Berlin

Scarano F (2013) Tomographic PIV: principles and practice. Meas Sci Technol 24:012001

Scarano F, Ghaemi S, Caridi GCA, Bosbach J, Dierksheide U, Sciacchitano A (2015) On the use of helium-filled soap bubbles for large-scale tomographic PIV in wind tunnel experiments. Exp Fluids 56:42

Terra W, Sciacchitano A, Scarano F (2017) Aerodynamic drag of a transitioning sphere by large-scale tomographic-PIV. Exp Fluids 58:83

Tropea C, Yarin AL, Foss J (2007) *Handbook of Experimental Fluid Mechanics*. Springer, Berlin, Germany